ACS Macro Letters

pubs.acs.org/macroletters Letter

# Mechanisms of Asymmetric Membrane Formation in Nonsolvent-Induced Phase Separation

Jan Ulric Garcia, Tatsuhiro Iwama, Eva Y. Chan, Douglas R. Tree, Kris T. Delaney, and Glenn H. Fredrickson*

Cite This: ACS Macro Lett. 2020, 9, 1617−1624 Read Online

ACCESS | Metrics & More | Article Recommendations | Supporting Information

**ABSTRACT:** We report the first simulations of nonsolvent-induced phase separation (NIPS) that predict membrane microstructures with graded asymmetric pore size distribution. In NIPS, a polymer solution film is immersed in a nonsolvent bath, enriching the film in nonsolvent, and leading to phase separation that forms a solid polymer-rich membrane matrix and polymer-poor membrane pores. We demonstrate how mass-transfer-induced spinodal decomposition, thermal fluctuations, and glass-transition dynamics—implemented with mobility contrast between the polymer-rich and polymer-poor phases—are essential to the formation of asymmetric membrane microstructures. Specifically, we show that the competition between the propagation of the phase-separation and glass-transition fronts determines the degree of pore-size asymmetry. We also explore the sensitivity of these microstructures to the initial film composition, and compare their formation in 2D and 3D.

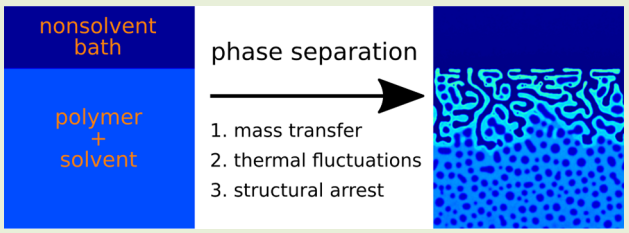


Polymer membranes are essential to water security: they purify our drinking water, desalinate seawater into potable water, and treat wastewater before its release to the environment.[1,2] The separation performance of these membranes is largely determined by their microstructure. An asymmetric microstructure is advantageous for many applications:[3] the smaller pores on the feed side of the membrane enable separation, while larger pores deeper into the membrane provide mechanical support with minimal resistance to permeate flow. Nonsolvent-induced phase separation (NIPS)[4,5]—also known as "wet-phase inversion" or the "Loeb−Sourirajan process"[6]—is a typical way to make asymmetric membranes. In NIPS, a homogeneous polymer solution is cast into a film and then immersed in a nonsolvent bath. The exchange of nonsolvent and solvent between the bath and the film enriches the film in nonsolvent, inducing phase separation of the film to a polymer-rich phase that becomes the membrane matrix and a polymer-poor phase that becomes the membrane pores.

Selecting process parameters to target specific membrane microstructures is challenging due to our limited understanding of NIPS; membrane manufacturers rely on heuristics, but this approach limits the development of more effective membranes. To understand NIPS, several research groups have modeled the NIPS system with Flory−Huggins thermodynamics coupled to multicomponent transport equations. Numerical techniques used to simulate NIPS include lattice

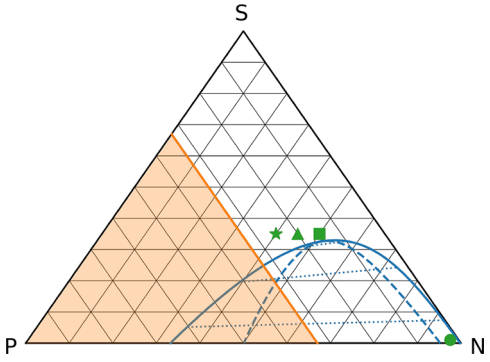


**Figure 1.** Ternary phase diagram for our NIPS system. Each vertex corresponds to pure polymer (P), pure solvent (S), and pure nonsolvent (N) compositions. The solid blue line marks the binodal while the dashed blue line marks the spinodal, as calculated with Flory−Huggins thermodynamics where $\chi_{pn} = 1.048$, $\chi_{ps} = \chi_{ns} = 0$, $N_p = 20$, $N_n = N_s = 1$. The dotted blue lines are examples of tie lines. The solid orange line marks the glass transition concentration, $\phi_p^* = 0.33$. Any composition within the shaded orange area is considered "glassy". The green circle marks the bath composition, which is almost pure nonsolvent ($\phi_p = 0.02$, $\phi_n = 0.97$). The green star ($\phi_p = 0.25$, $\phi_n = 0.40$), green triangle ($\phi_p = 0.20$, $\phi_n = 0.45$), and green square ($\phi_p = 0.15$, $\phi_n = 0.50$) mark the initial homogeneous film compositions used in this study.

Received: August 19, 2020
Accepted: October 19, 2020
Published: October 26, 2020

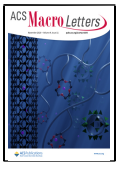






https://dx.doi.org/10.1021/acsmacrolett.0c00609
ACS Macro Lett. 2020, 9, 1617−1624

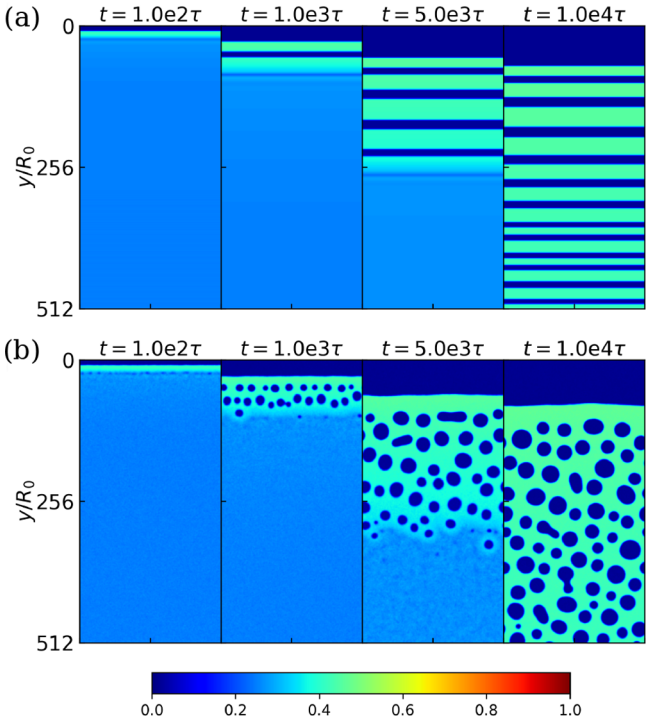


**Figure 2.** NIPS simulations (a) without ($\alpha$ = 0) and (b) with ($\alpha$ = 0.04) thermal fluctuations. Each box shown is $256R_0 \times 512R_0$. The $y$-coordinate corresponds to film depth, where $y$ = 0 is the film−bath interface and $y$ = 512 is the bottom of the film. The bath is not visualized for clarity. Polymer-rich regions are light green and polymer-poor regions are dark blue; color bar included for $\phi_p$. Initial film composition is ($\phi_p$ = 0.25, $\phi_n$ = 0.40), corresponding to the green star in Figure 1. No glass transition effects are introduced, i.e., $\eta_p/\eta_s$ = 1 for both (a) and (b).

Boltzmann,[7] smoothed particle hydrodynamics,[8] and phase-field simulations.[9−12] While these studies have shown mass-transfer-induced phase separation, they predicted either the unrealistic formation of alternating polymer-rich and polymer-poor layers aligned with the film−bath interface, or the formation of microstructures with homogeneous pore size distributions. To our knowledge, no existing numerical study of NIPS has shown the formation of graded asymmetric pore size distributions, suggesting that physics essential to NIPS membrane formation is missing in the existing models. In their numerical study of membrane formation by thermally induced phase separation (TIPS), Millett and co-workers[13] demonstrated the formation of graded asymmetric microstructures by anisotropic cooling of a homogeneous film into a phase-separated membrane. Based on their TIPS model and the NIPS studies mentioned above, we hypothesize that in addition to mass-transfer-induced phase separation, two more mechanisms are essential to the formation of asymmetric microstructures: thermal fluctuations and structural arrest due to solidification of the polymer-rich phase. Solidification mechanisms[14] in NIPS include crystallization, gelation, and vitrification; we select glassy dynamics for the solidification mechanism in this study.

We have modified our phase-field model from previous NIPS studies[10−12] to incorporate thermal fluctuations and a glass transition. To focus on these two features, we exclude hydrodynamics in this study and use a system of diffusion equations to model NIPS. Hydrodynamics are discussed further in the Supporting Information. Using $R_0$, the root-mean-square (RMS) end-to-end distance of a reference polymer with degree of polymerization $N_r$ as the characteristic length scale, $\tau$, the Rouse time of the reference polymer in a solvent of viscosity, $\eta_s$, as the characteristic time scale, and $N_r k_B T/b^3$ as the characteristic chemical potential scale, we present our model in dimensionless form:

$$\frac{\partial \phi_i(\boldsymbol{r}, t)}{\partial t} = \nabla\cdot\left[\sum_j^{p,n} M_{ij}(\{\phi_i\})\nabla\mu_j(\{\phi_i\})\right] + \alpha N_r^{-1/4}\theta_i(\boldsymbol{r}, t) \tag{1}$$

where $\phi_p(\boldsymbol{r},t)$ and $\phi_n(\boldsymbol{r},t)$ are the polymer and nonsolvent volume fractions, $M_{ij}$ is the mobility matrix, $\mu_j$ is the chemical potential of species $j$, and $\theta_i(\boldsymbol{r},t)$ are noise terms that follow fluctuation−dissipation theorem (FDT) statistics,[15]

$$\langle\theta_i(\boldsymbol{r}, t)\rangle = 0 \tag{2a}$$

$$\langle\theta_i(\boldsymbol{r}, t)\theta_j(\boldsymbol{r}', t')\rangle = -2\nabla\cdot[M_{ij}(\{\phi_i\})\nabla\delta(\boldsymbol{r} - \boldsymbol{r}')]\delta(t - t') \tag{2b}$$

The incompressibility assumption implicitly gives the solvent volume fraction, $\phi_s = 1 - \phi_p - \phi_n$. The noise-scaling factor, $\alpha \in [0,1]$, reduces the strength of the fluctuations in eq 1 for numerical stability, where $\alpha$ = 0 makes the dynamics purely deterministic, while $\alpha$ = 1 sets noise strengths consistent with FDT. For all stochastic simulations in this work, we set $\alpha$ = 0.04; although this value breaks consistency with FDT, we show that $\alpha$ = 0.04 is large enough to eliminate nonphysical membrane features observed in purely deterministic simulations. A glass transition is introduced in the model through the use of concentration-dependent mobilities,

$$M_{pp} = \phi_p(1 - \phi_p)/\eta \tag{3a}$$

$$M_{pn} = M_{np} = -\phi_p\phi_n/\eta \tag{3b}$$

$$M_{nn} = \phi_n(1 - \phi_n)/\eta \tag{3c}$$

where $\eta$ is the concentration-dependent local viscosity. We confer glassy dynamics by modeling $\eta$ as a sigmoidal function of the local polymer volume fraction, $\phi_p(\boldsymbol{r})$:

$$\eta = 1 + \frac{\eta_p/\eta_s - 1}{1 + \exp\left(-\frac{1}{w}(\phi_p(\boldsymbol{r}) - \phi_p^*)\right)} \tag{4}$$

where $\eta_p/\eta_s$ represents the pure-component viscosity ratio of the polymer and the solvent (implicitly assuming $\eta_n = \eta_s$), $w$ controls the width of the sigmoid, and $\phi_p^*$ represents the glass-transition concentration. A sigmoid mimics the Vogel−Fulcher−Tamman−Hesse (VFTH) and Williams−Landel−Ferry (WLF) equations[16] with the exponential growth of viscosity, while bounding its maximum value for computational stability. Setting $w = 5 \times 10^{-3}$ approximates $\eta$ as a step function, narrow enough such that $\eta$ = 1 at $\phi_p$ = 0, but wide enough to avoid computational issues associated with a mathematical discontinuity. This choice implies that for $\phi_p$ values far enough from $\phi_p^*$, $\eta$ = 1 for $\phi_p(\boldsymbol{r}) < \phi_p^*$, while $\eta = \eta_p/\eta_s$ for $\phi_p(\boldsymbol{r}) > \phi_p^*$. Thus, local mobilities are unscaled in non-glassy regions but they are scaled by $\eta_p/\eta_s$ in glassy regions. Setting $\eta_p/\eta_s$ = 1 disables the glass transition while $\eta_p/\eta_s = 1 \times 10^4$ enables it. The latter value serves as a balance between faithfully representing a physical glass transition and accessing


https://dx.doi.org/10.1021/acsmacrolett.0c00609
ACS Macro Lett. 2020, 9, 1617−1624

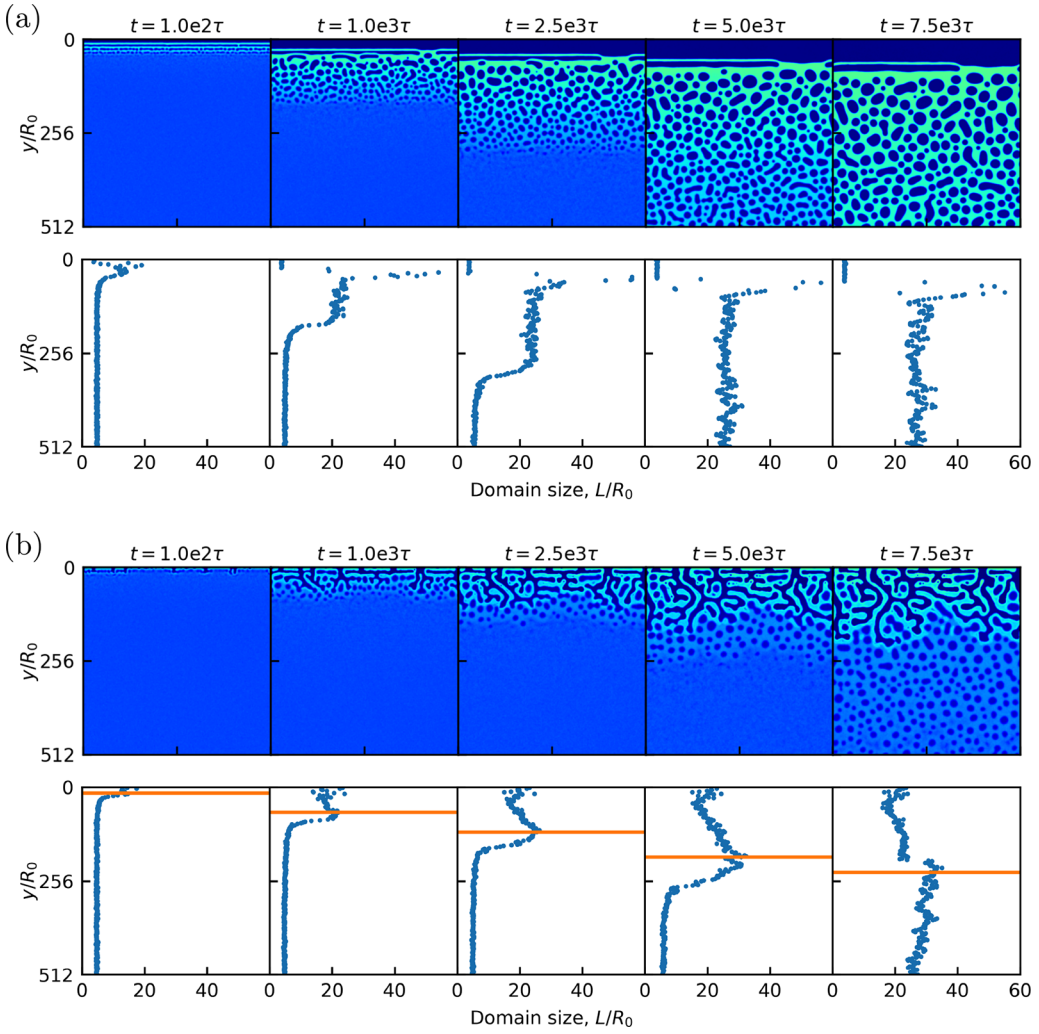


**Figure 3.** NIPS simulations in 2D and their domain size profiles (a) without and (b) with glass transition effects for the initial film composition of ($\phi_p$ = 0.20, $\phi_n$ = 0.45), corresponding to the green triangle in Figure 1. Mobility contrasts set at (a) $\eta_p/\eta_s$ = 1, (b) $\eta_p/\eta_s$ = $10^4$. Each density plot shown is $512R_0 \times 512R_0$. The $y$-coordinate corresponds to film depth, where $y$ = 0 is the film−bath interface and $y$ = 512 is the bottom of the film. The bath is not visualized for clarity. Polymer-rich regions are light green and polymer-poor regions are dark blue; $\phi_p$ color bar included in Figure 2. The orange line (glass-transition front) in the domain size profile for (b) corresponds to the deepest point in the film where at least one grid point has crossed the glass transition concentration, $\phi_p^*$.

practical simulation times; we further justify this choice in the Supporting Information.

Finally, the chemical potential terms in eq 1 are calculated as the functional derivatives of the system free energy, $\mu_i = \delta F/\delta\phi_i$, where Flory−Huggins−de Gennes thermodynamics describe the free energy:

$$F[\{\phi_i\}] = \int \mathrm{d}\mathbf{r}[f(\{\phi_i\}) + g(\{\phi_i\})] \tag{5a}$$

$$f(\{\phi_i\}) = \sum_i^{p,n,s} \frac{\phi_i}{N_i} \ln \phi_i + \frac{1}{2} \sum_{i\neq j}^{p,n,s} \chi_{ij}\phi_i\phi_j \tag{5b}$$

$$g(\{\phi_i\}) = \frac{1}{2}[\nabla\phi_p \nabla\phi_n] \begin{bmatrix} \kappa_p + \kappa_s & \kappa_s \\ \kappa_s & \kappa_n + \kappa_s \end{bmatrix} \begin{bmatrix} \nabla\phi_p \\ \nabla\phi_n \end{bmatrix} \tag{5c}$$

Equations 5b and 5c represent the bulk and interfacial free energy contributions, respectively. We set the degree of polymerization of each component as, $N_p$ = 20, $N_n$ = $N_s$ = 1, with the reference, $N_r$ = 20, the interaction parameters as $\chi_{pn}$ = 1.048, $\chi_{ps}$ = $\chi_{ns}$ = 0, and the square-gradient coefficients as $\kappa_p$ = $\kappa_n$ = $\kappa_s$ = 1.5. We provide further details of our model and numerical methods in the Supporting Information.

Figure 1 shows the ternary phase diagram for the NIPS system in this work. We set initial film compositions near the critical point based on our findings that such compositions are necessary for mass-transfer-induced phase separation.[12] The nonsolvent bath composition was set to nearly pure nonsolvent, leaving only small amounts of polymer and solvent to avoid the singular composition bounds of the Flory−Huggins functional. We initialized the top-half of the simulation box as the bath and the bottom-half as the homogeneous film. No-flux boundary conditions were implemented at the bottom of the film and at the top of the bath, while periodic boundary conditions were imposed on the lateral sides of the simulation box. To visualize results, only domains corresponding to the initial homogeneous film were shown, omitting the nonsolvent bath for clarity. The glass-transition concentration was set to $\phi_p^*$ = 0.33, a value close enough to the initial film compositions so that mobility contrast effects manifest soon after phase separation. In reality, $\phi_p^*$ is not arbitrary, as it changes with


https://dx.doi.org/10.1021/acsmacrolett.0c00609
ACS Macro Lett. 2020, 9, 1617−1624

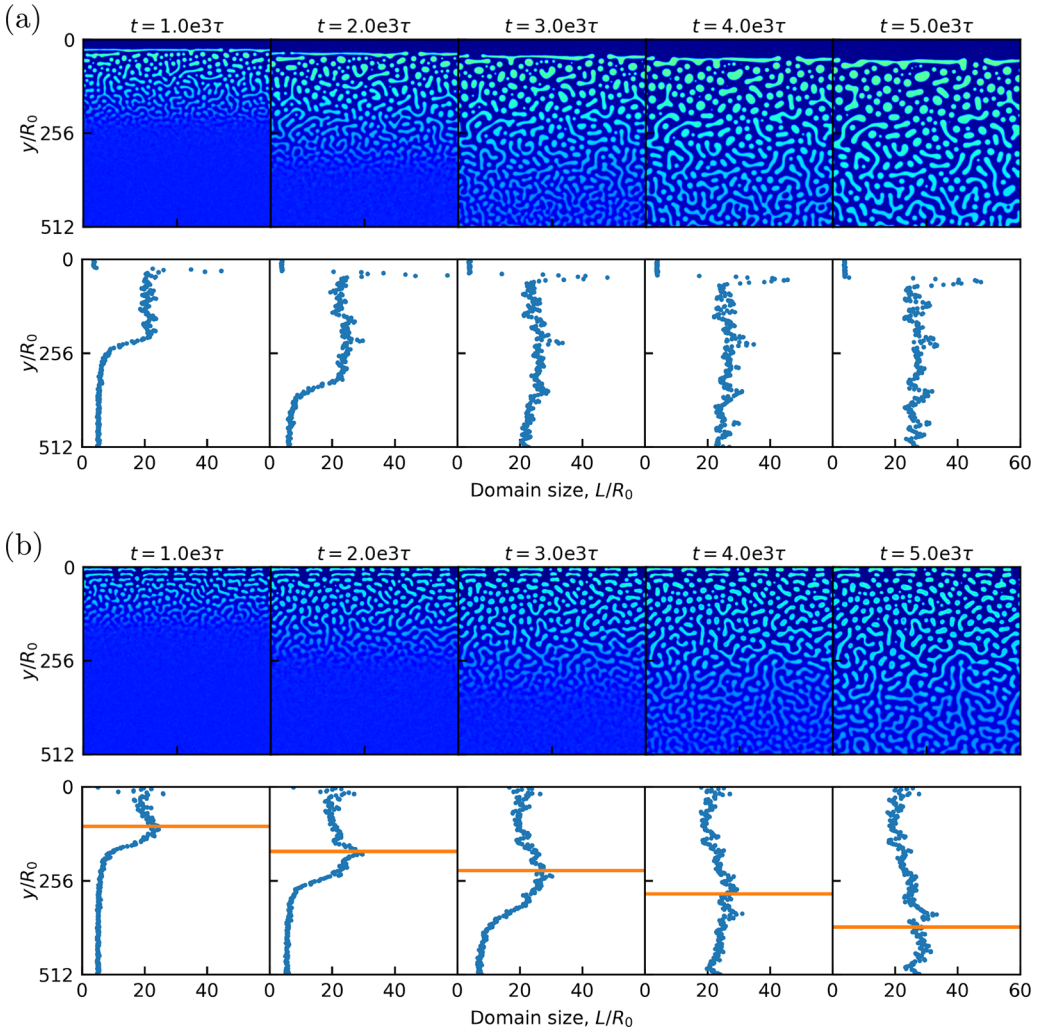


**Figure 4.** NIPS simulations in 2D and their domain size profiles (a) without and (b) with glass transition effects for the initial film composition of ($\phi_p$ = 0.15, $\phi_n$ = 0.50), corresponding to the green square in Figure 1. Mobility contrasts set at (a) $\eta_p/\eta_s$ = 1, (b) $\eta_p/\eta_s$ = $10^4$. Each density plot shown is $512R_0 \times 512R_0$. The $y$-coordinate corresponds to film depth, where $y$ = 0 is the film−bath interface and $y$ = 512 is the bottom of the film. The bath is not visualized for clarity. Polymer-rich regions are light green and polymer-poor regions are dark blue; $\phi_p$ color bar included in Figure 2. The orange line (glass-transition front) in the domain size profile for (b) corresponds to the deepest point in the film where at least one grid point has crossed the glass transition concentration, $\phi_p^*$.

dope formulation and temperature.[17,18] We leave the effects of varying $\phi_p^*$ to future work.

Figure 2 illustrates the effects of thermal fluctuations on mass-transfer-driven microstructure evolution. In the absence of fluctuations (Figure 2a), a pattern of alternating polymer-rich and polymer-poor layers forms parallel to the film−bath interface, consistent with other numerical studies of NIPS.[8,12] We attribute the propagation of the ordered pattern to surface-directed spinodal decomposition (SDSD).[19] In contrast, enabling fluctuations (Figure 2b) introduces disorder to the dynamics, disrupting the propagation of this ordered pattern with more isotropic bulk spinodal decomposition. The two rows of polymer-poor circles at $t = 1 \times 10^3$, manifest the competition between the order imposed by SDSD and the disorder due to thermal fluctuations. Morphologies at later times show that deeper into the film, the influence of SDSD wanes and bulk spinodal decomposition dominates. As shown, setting $\alpha$ = 0.04 is enough to break the ordered pattern, but the effects of stronger fluctuations, including phase separation by nucleation, remain unexplored; we leave this complexity to future work.

Figure 3 shows the effects of the glass transition on the 2D microstructure. In the absence of a glass transition (Figure 3a), the progress of microstructure formation varies with film depth at early times (first three frames). A phase-separation front due to SDSD follows nonsolvent diffusion into the film. Just above the phase-separation front, domain sizes increase toward the film−bath interface; but far enough from the front, domain sizes become more homogeneous, a profile that eventually manifests through the whole film at late times (last two frames). We attribute these observations to domain coarsening. In a bulk quench of a system that coarsens only by diffusion, the characteristic domain size, $L$, follows the Lifshitz−Slyozov−Wagner[20,21] scaling law, $L \sim t^{1/3}$. Assuming that a similar power law applies to mass-transfer-induced phase separation, i.e., the coarsening mechanisms involved do not change the exponent, we posit that for phase-separated domains,

$$L(t, y) \sim (t - t_p(y))^{1/3} \quad (6)$$



https://dx.doi.org/10.1021/acsmacrolett.0c00609
ACS Macro Lett. 2020, 9, 1617−1624

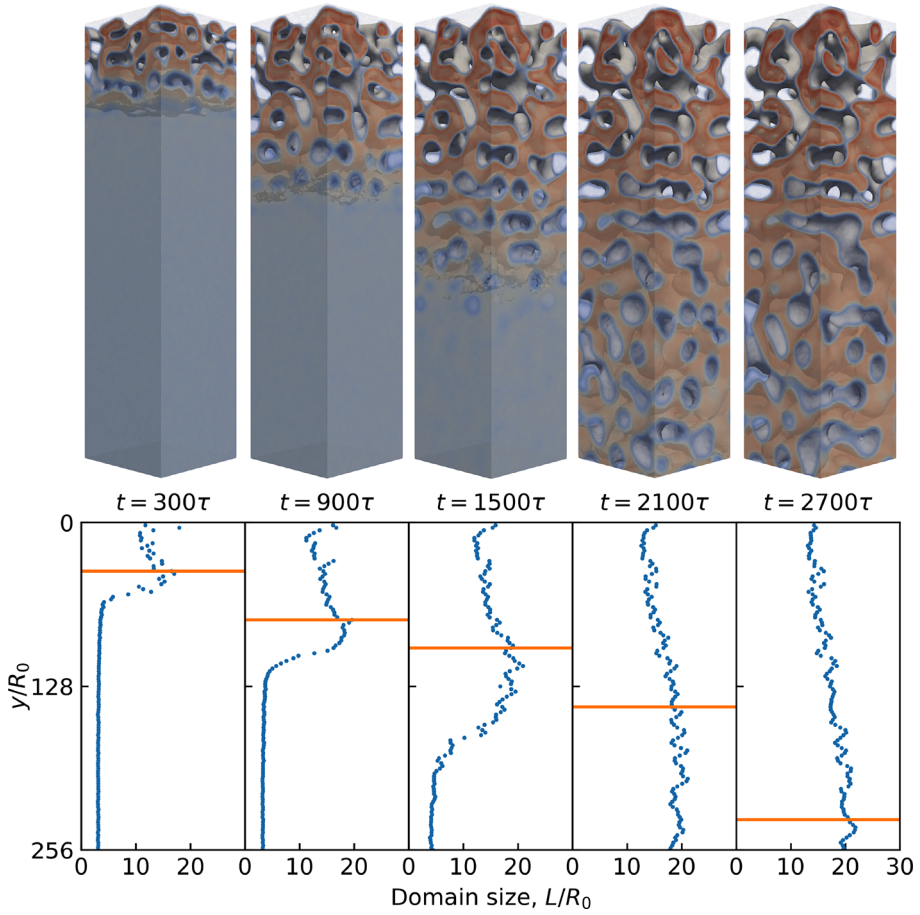


**Figure 5.** NIPS simulation in 3D and its domain size profile for the initial film composition of ($\phi_p$ = 0.20, $\phi_n$ = 0.45), corresponding to the green triangle in Figure 1. Mobility contrast set at $\eta_p/\eta_s = 10^4$. Each density plot shown is $64R_0 \times 256R_0 \times 64R_0$. The $y$-coordinate corresponds to film depth, where $y = 0$ is the film−bath interface and $y = 256$ is the bottom of the film. The bath is not visualized for clarity. Polymer-rich regions are opaque red, polymer-poor regions are translucent blue, and the isosurface is opaque beige. The orange line (glass-transition front) in the domain size profile corresponds to the deepest point in the film where at least one grid point has crossed the glass transition concentration, $\phi_p^*$.

where $t_p(y)$ is the time when the phase-separation front arrived at film depth, $y$. Equation 6 offers a crude rationalization for our simulations since phase-separated domains in 2D span several values of $y$; nevertheless, it proves useful for the discussion. For domains just above the phase-separation front, the quantity $(t - t_p(y))$ increases away from the front, consistent with the observed domain-size profile. However, for domains far enough from the phase-separation front, we can approximate $(t - t_p(y)) \approx t$, implying $L$ is no longer a function of film depth for these mature domains. The same approximation applies to all values of $y$, long after the phase separation front has reached the bottom of the film, explaining the symmetric pore-size distribution at late times. We discuss the computation of the average domain size for each $y$-slice in the Supporting Information.

In contrast, the glass transition dramatically changes the microstructure (Figure 3b). To begin, a polymer-rich skin forms at the film−bath interface. Thermal fluctuations introduce perforations on the polymer-rich skin before it turns glassy. Due to the imposed mobility contrast, the glassy skin then acts as a barrier to nonsolvent entry, only allowing the nonsolvent to penetrate the film through the perforations, consistent with the proposed mechanism by Smolders and co-workers.[22−24] The perforations grow deeper into the film, forming finger-like structures that eventually become a network of pores—a stark contrast from the closed-pore morphology formed without the glass transition. Though similar in appearance, these "finger-like structures" are distinct from macrovoids[25,26] that span the thickness of a membrane; we make no claims about macrovoid formation in this work.

In addition to the qualitative change in morphology, the glass transition also leads to a positive pore-size gradient from the film−bath interface to the glass-transition front, evidenced by the positive slope of the film-depth vs domain-size curve from $y = 0$ to the orange glass-transition line. *The mechanism responsible for this pore-size gradient is the increasing lead of the phase-separation front over the glass-transition front.* We plot the propagation dynamics of these two fronts in the Supporting Information. Domain features above the glass-transition front are frozen while those below it are free to evolve. Following the same assumptions made for eq 6, we posit that for domains above the glass-transition front:

$$L(y) \sim (t_g(y) - t_p(y))^{1/3} \tag{7}$$

where $t_g(y)$ and $t_p(y)$ are the times when the glass-transition and phase-separation fronts arrived at film depth, $y$, respectively. Again, eq 7 offers a crude rationalization for our simulations, but it proves useful for the discussion. Since the phase-separation front moves faster than the glass-transition front, the quantity $(t_g(y) - t_p(y))$ increases with film depth,


https://dx.doi.org/10.1021/acsmacrolett.0c00609
ACS Macro Lett. 2020, 9, 1617−1624

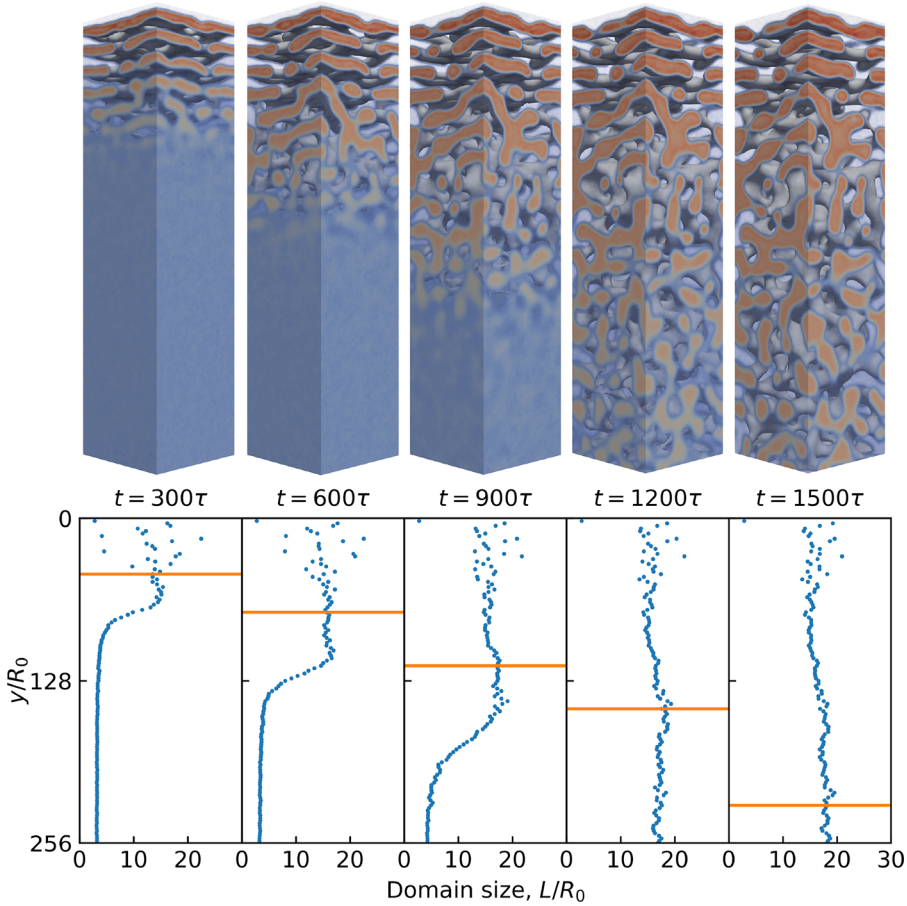


**Figure 6.** NIPS simulation in 3D and its domain size profile for the initial film composition of ($\phi_p$ = 0.15, $\phi_n$ = 0.50), corresponding to the green square in Figure 1. Mobility contrast set at $\eta_p/\eta_s = 10^4$. Each density plot shown is $64R_0 \times 256R_0 \times 64R_0$. The $y$-coordinate corresponds to film depth, where $y = 0$ is the film−bath interface and $y = 256$ is the bottom of the film. The bath is not visualized for clarity. Polymer-rich regions are opaque red, polymer-poor regions are translucent blue, and the isosurface is opaque beige. The orange line (glass-transition front) in the domain size profile corresponds to the deepest point in the film where at least one grid point has crossed the glass transition concentration, $\phi_p^*$.

leading to the asymmetric pore-size distribution. This proposed mechanism is not unfounded; using in-situ experiments, McHugh and co-workers[27] correlated the transition from a macrovoid morphology to a sponge microstructure with changes to the propagation dynamics of these two fronts, demonstrating their importance to shaping membrane morphology.

While Figure 3 shows microstructures with a continuous polymer-rich phase, Figure 4 demonstrates that less polymer content in the initial film can lead to an inversion of the continuous phase to polymer-poor. In the absence of a glass transition (Figure 3a vs Figure 4a), the inversion itself does not change the propagation kinetics of the phase-separation front; the front in Figure 4a has a slight lead in penetrating the film only because its initial film composition is closer to the binodal, allowing nonsolvent entry to induce phase separation earlier. On the other hand, the inversion alters front-propagation dynamics in the presence of a glass transition (Figure 3b vs Figure 4b). Since the polymer-poor phase is continuous in Figure 4b, nonsolvent can penetrate the film without having to form finger-like structures, allowing both the phase-separation and glass-transition fronts to propagate more quickly. However, this speed-up unevenly favors the glass-transition front, effectively reducing $(t_g(y) - t_p(y))$ for frozen domains. As a consequence, the domain-size gradient from the film−bath interface to the glass-transition front becomes less pronounced in Figure 4b than it was for Figure 3b.

The dynamics of membrane formation also change in 3D, owing to the greater tendency of domains to stay continuous after phase separation. Figure 5 shows the 3D equivalent of Figure 3b. The finger-like structures in 2D translate to a 3D pore network that allows the nonsolvent to penetrate the film faster in 3D. The bicontinuous microstructure in 3D leads to speed-ups for both the phase-separation and glass-transition fronts. Again, the speed-up unevenly favors the latter—especially for deeper points in the film—leading to a less-pronounced gradient in domain size for the 3D microstructure.

Similar effects of bicontinuity are shown in Figure 6, the 3D equivalent of Figure 4b. The discrete polymer-rich phase in the 2D morphology translates to a mostly continuous structure in 3D. Despite the continuous polymer-rich phase, the higher dimensionality still leads to speed-ups for both the phase-separation and glass-transition fronts. The domain-size gradient in 3D is again less-pronounced due to the larger speed-up of the glass-transition front.

Despite the bicontinuity of both 3D morphologies (Figure 5 vs Figure 6), initial film composition remains important to the propagation of the phase-separation and glass-transition fronts. Less polymer content in the initial film leads to less resistance to mass-transfer, evidenced by faster propagation of both fronts in Figure 6. However, the faster advance of both fronts also


https://dx.doi.org/10.1021/acsmacrolett.0c00609
ACS Macro Lett. 2020, 9, 1617−1624

leads to less pronounced domain-size asymmetry, as demonstrated by the decreased slope in the film-depth vs domain-size curve in Figure 6.

While the asymmetric structures observed here in both 2D and 3D are in qualitative agreement with experiments,[28,29] we do not attempt quantitative comparisons. Instead, our focus was on gaining a mechanistic understanding of NIPS by building a model step-by-step, adding complexity in each step and considering its role in membrane formation. We demonstrated that mass-transfer-induced phase separation, thermal fluctuations, and a structural arrest mechanism are necessary and sufficient to form graded asymmetric pore-size distributions. However, other complexities in experiments remain unexplored, notably hydrodynamics. As velocities are scaled by the inverse of mixture viscosity, we assume that flows in any continuous polymer-rich phase are negligible, due to the high viscosity ratio in our glassy dynamics model. Evidence for this assumption is provided in the Supporting Information. Of course, hydrodynamics can prove to be more significant in NIPS operating regimes where the continuous polymer-rich phase is not subject to early vitrification; such complexities, including the physical mechanisms behind the formation of macrovoids[25,26] and other membrane morphologies,[30,31] are left to future study.

**Note:** After we submitted this manuscript for publication, we became aware of an article in press[32] that uses a NIPS model similar to our own, but targeted at a specific polymer−solvent−nonsolvent system.

## ■ ASSOCIATED CONTENT

### Supporting Information

The Supporting Information is available free of charge at https://pubs.acs.org/doi/10.1021/acsmacrolett.0c00609.

> Phase-field model and numerical methods; derivation of the fluctuation scales; simulation setup; pore size analysis; porosity analysis; choosing the mobility contrast $\eta_p/\eta_s$; formation of the finger-like structures in 2D; propagation dynamics of the phase-separation and glass-transition fronts; phase separation with hydrodynamics (PDF)

## ■ AUTHOR INFORMATION


### Corresponding Author

**Glenn H. Fredrickson** − *Department of Chemical Engineering, Materials Research Laboratory, and Department of Materials, University of California, Santa Barbara, California 93106, United States;* orcid.org/0000-0002-6716-9017; Email: ghf@ucsb.edu

### Authors

**Jan Ulric Garcia** − *Department of Chemical Engineering and Materials Research Laboratory, University of California, Santa Barbara, California 93106, United States;* orcid.org/0000-0003-1918-2468

**Tatsuhiro Iwama** − *Asahi Kasei Corporation, Fuji, Shizuoka 416-8501, Japan*

**Eva Y. Chan** − *Department of Chemical Engineering, University of California, Santa Barbara, California 93106, United States;* orcid.org/0000-0002-0246-3901

**Douglas R. Tree** − *Department of Chemical Engineering, Brigham Young University, Provo, Utah 84602, United States;* orcid.org/0000-0002-1412-0244

**Kris T. Delaney** − *Materials Research Laboratory, University of California, Santa Barbara, California 93106, United States;* orcid.org/0000-0003-0356-1391

Complete contact information is available at: https://pubs.acs.org/10.1021/acsmacrolett.0c00609


### Notes

The authors declare no competing financial interest.

## ■ ACKNOWLEDGMENTS

We acknowledge financial support from Asahi Kasei Corporation, from the Center for Materials for Water and Energy Systems (MWET), an Energy Frontier Research Center funded by the U.S. Department of Energy, Office of Science, Basic Energy Sciences under Award No. DE-SC0019272, and from Brigham Young University. We acknowledge computational resources from the Center for Scientific Computing from the CNSI, and MRL: a National Science Foundation (NSF) Materials Research Science and Engineering Center (MRSEC) (DMR-1720256) and NSF CNS-1725797. J.U.G. acknowledges financial support from the Natural Sciences and Engineering Research Council of Canada (NSERC) PGS-D scholarship program. We thank Prof. Hector D. Ceniceros (UC Santa Barbara) for helpful discussions regarding the numerical treatment of fluctuating simulations.

## ■ REFERENCES


(1) Pendergast, M. M.; Hoek, E. M. A review of water treatment membrane nanotechnologies. *Energy Environ. Sci.* **2011**, *4*, 1946−1971.

(2) Landsman, M. R.; et al. Water Treatment: Are Membranes the Panacea? *Annu. Rev. Chem. Biomol. Eng.* **2020**, *11*, 559−585.

(3) Baker, R. W. *Membrane Technology and Applications*, 3rd ed.; John Wiley and Sons, Ltd.: West Sussex, UK, 2012; pp 1−571.

(4) Guillen, G. R.; Pan, Y.; Li, M.; Hoek, E. M. V. Preparation and Characterization of Membranes Formed by Nonsolvent Induced Phase Separation: A Review. *Ind. Eng. Chem. Res.* **2011**, *50*, 3798−3817.

(5) Wang, D.-M.; Lai, J.-Y. Recent advances in preparation and morphology control of polymeric membranes formed by nonsolvent induced phase separation. *Curr. Opin. Chem. Eng.* **2013**, *2*, 229−237.

(6) Loeb, S.; Sourirajan, S. High flow porous membranes for separating water from saline solutions. U.S. Patent 3,133,132, 1964.

(7) Akthakul, A.; Scott, C. E.; Mayes, A. M.; Wagner, A. J. Lattice Boltzmann simulation of asymmetric membrane formation by immersion precipitation. *J. Membr. Sci.* **2005**, *249*, 213−226.

(8) Hopp-Hirschler, M.; Nieken, U. Modeling of pore formation in phase inversion processes: Model and numerical results. *J. Membr. Sci.* **2018**, *564*, 820−831.

(9) Zhou, B.; Powell, A. C. Phase field simulations of early stage structure formation during immersion precipitation of polymeric membranes in 2D and 3D. *J. Membr. Sci.* **2006**, *268*, 150−164.

(10) Tree, D. R.; Delaney, K. T.; Ceniceros, H. D.; Iwama, T.; Fredrickson, G. H. A multi-fluid model for microstructure formation in polymer membranes. *Soft Matter* **2017**, *13*, 3013−3030.

(11) Tree, D. R.; Iwama, T.; Delaney, K. T.; Lee, J.; Fredrickson, G. H. Marangoni Flows during Nonsolvent Induced Phase Separation. *ACS Macro Lett.* **2018**, *7*, 582−586.

(12) Tree, D. R.; Dos Santos, L. F.; Wilson, C. B.; Scott, T. R.; Garcia, J. U.; Fredrickson, G. H. Mass-transfer driven spinodal decomposition in a ternary polymer solution. *Soft Matter* **2019**, *15*, 4614−4628.

(13) Cervellere, M. R.; Tang, Y.; Qian, X.; Ford, D. M.; Millett, P. C. Mesoscopic simulations of thermally-induced phase separation in PVDF/DPC solutions. *J. Membr. Sci.* **2019**, *577*, 266.

(14) van de Witte, P.; Dijkstra, P. J.; van den Berg, J. W. a.; Feijen, J. Phase separation processes in polymer solutions in relation to membrane formation. *J. Membr. Sci.* **1996**, *117*, 1−31.
(15) Hohenberg, P. C.; Halperin, B. I. Theory of dynamic critical phenomena. *Rev. Mod. Phys.* **1977**, *49*, 435−479.
(16) Hiemenz, P. C.; Lodge, T. P. *Polymer Chemistry*, 2nd ed.; CRC Press: Boca Raton, FL, 2007; pp 1−575.
(17) Li, S.-G.; van den Boomgaard, T.; Smolders, C. A.; Strathmann, H. Physical gelation of amorphous polymers in a mixture of solvent and nonsolvent. *Macromolecules* **1996**, *29*, 2053−2059.
(18) Kim, J. Y.; Kim, Y. D.; Kanamori, T.; Lee, H. K.; Baik, K.-j.; Kim, S. C. Vitrification Phenomena in Polysulfone/NMP/Water System. *J. Appl. Polym. Sci.* **1999**, *71*, 431−438.
(19) Ball, R. C.; Essery, R. L. Spinodal decomposition and pattern formation near surfaces. *J. Phys.: Condens. Matter* **1990**, *2*, 10303−10320.
(20) Lifshitz, I.; Slyozov, V. The kinetics of precipitation from supersaturated solid solutions. *J. Phys. Chem. Solids* **1961**, *19*, 35−50.
(21) Wagner, C. Theorie der alterung von niederschlagen durch umlosen (Ostwald-reifung). *Z. Elektrochem.* **1961**, *65*, 581−591.
(22) Koenhen, D. M.; Mulder, M. H. V.; Smolders, C. A. Phase separation phenomena during the formation of asymmetric membranes. *J. Appl. Polym. Sci.* **1977**, *21*, 199−215.
(23) Wijmans, J. G.; Baaij, J. P. B.; Smolders, C. A. The mechanism of formation of microporous or skinned membranes produced by immersion precipitation. *J. Membr. Sci.* **1983**, *14*, 263−274.
(24) Wijmans, J.G; Kant, J; Mulder, M. H. V.; Smolders, C.A Phase separation phenomena in solutions of polysulfone in mixtures of a solvent and a nonsolvent: relationship with membrane formation. *Polymer* **1985**, *26*, 1539−1545.
(25) Smolders, C. A.; Reuvers, A. J.; Boom, R. M.; Wienk, I. M. Microstructures in phase-inversion membranes. Part 1. Formation of macrovoids. *J. Membr. Sci.* **1992**, *73*, 259−275.
(26) Wang, H. H.; Jung, J. T.; Kim, J. F.; Kim, S.; Drioli, E.; Lee, Y. M. A novel green solvent alternative for polymeric membrane preparation via nonsolvent-induced phase separation (NIPS). *J. Membr. Sci.* **2019**, *574*, 44−54.
(27) McHugh, A. J.; Tsay, C. S. Dynamics of the Phase Inversion Process. *J. Appl. Polym. Sci.* **1992**, *46*, 2011−2021.
(28) Strathmann, H.; Kock, K.; Amar, P.; Baker, R. W. The formation mechanism of asymmetric membranes. *Desalination* **1975**, *16*, 179−203.
(29) Radovanovic, P.; Thiel, S. W.; Hwang, S. T. Formation of asymmetric polysulfone membranes by immersion precipitation. Part II. The effects of casting solution and gelation bath compositions on membrane structure and skin formation. *J. Membr. Sci.* **1992**, *65*, 231−246.
(30) Cardoso, V. F.; Botelho, G.; Lanceros-Méndez, S. Nonsolvent induced phase separation preparation of poly(vinylidene fluoride-co-chlorotrifluoroethylene) membranes with tailored morphology, piezoelectric phase content and mechanical properties. *Mater. Des.* **2015**, *88*, 390−397.
(31) Jung, J. T.; Kim, J. F.; Wang, H. H.; di Nicolo, E.; Drioli, E.; Lee, Y. M. Understanding the non-solvent induced phase separation (NIPS) effect during the fabrication of microporous PVDF membranes via thermally induced phase separation (TIPS). *J. Membr. Sci.* **2016**, *514*, 250−263.
(32) Cervellere, M. R.; Qian, X.; Ford, D. M.; Carbrello, C.; Giglia, S.; Millett, P. C. Phase-field modeling of non-solvent induced phase separation (NIPS) for PES/NMP/Water with comparison to experiments. *J. Membr. Sci.* **2021**, *619*, 118779.


https://dx.doi.org/10.1021/acsmacrolett.0c00609
*ACS Macro Lett.* 2020, 9, 1617−1624